Conceptual design of a beam extraction electrode system for a 1 mN ion thruster

G. M. Sandonato and J. J. Barroso

Laboratório Associado de Plasma, Instituto Nacional de Pesquisas Espaciais (INPE), 12.201-970,
São José dos Campos, SP, Brazil

Conceptual modeling of the multiaperture electrode system of a 5-cm-diam ring cusp ion thruster intended for producing a 1 mN thrust is described. A mathematical treatment of the ion extraction from the plasma has been developed to provide a method for calculating both the shape and potential of the plasma-emitting surface. The ion optics of the electrode system have been examined using a numerical code to evaluate the ion beam divergence. Close agreement is achieved between the predictions of the conceptual modeling presented here and published experimental results. © *1996 American Institute of Physics.* [S0034-6748(96)01603-6]

I. INTRODUCTION

Ion sources have found a broad range of applications including neutral beam injection in nuclear fusion research, microelectronics processing, and space technology.[1,2] In particular, due to the high exhaust velocity and the low propellant consumption, ion sources can be used to advantage as ion thrusters for attitude and orbit control of satellites.[2,3]

However, in small discharge chamber volumes, poor primary electron magnetic containment can prevent the ion thruster from achieving high efficiency as the primary electrons are quickly collected by the anode wall, thus increasing the discharge current required for plasma creation. The ion thruster lifetime is also reduced if the ion beam is not suitably produced by the electrode extraction system, since, in this case, the electrodes can be seriously damaged by ion erosion.

In this work a 5-cm-diam and 10-cm-long ion source has been devised for producing 1 mN thrust with a maximum overall power consumption of 50 W. The primary electron containment problem has been numerically investigated and an optimized ring cusp geometry has been found which yields a primary electron containment time as high as 65 μs.[4] This translates into a specific impulse of 2500 s with a propellant utilization of about 70% and a minimum electrical efficiency of 25%.

This paper deals with the design of ion beam extraction and acceleration grid systems of ion thrusters consistent with the plasma production in the discharge chamber. The location and shape of the ion-emitting surface are essentially dependent on the plasma parameters (density, potential, and electron temperature), electrode geometry, and applied voltages. This adds considerable complexity to the study of ion extraction from a plasma. A number of numerical codes have been developed previously to tackle this problem.[5–7]

By contrast, in our approach we propose a simple analytical model to determine the location and shape of the plasma sheath boundary. The ion beam extraction modeling is developed in Sec. II, where both the potential on the emitting surface and its distance from the extraction grid have been determined using the Poisson equation with a one-dimensional source term.

After exploring the interrelationship between the emitting-surface parameters and the geometry of the ion-optics system, an analytical design scheme is devised to optimize the multiaperture two-electrode system so as to generate a laminar ion beam. The ion beam trajectory has been determined using an adapted version of the Herrmannsfeldt's code (SLAC)[8,9] to check if the synthesized electrode system will produce the desired laminar ion beam.

An experimental ion thruster[10] validating our electrode system design method is presented in Sec. III, which also describes the beam optics of our 5 cm ion thruster. Finally, the results of the present study are discussed in Sec. IV.

II. ION BEAM MODELING

The ion beam was modeled assuming that the ring–cusp magnetic field shown in Fig. 1(a) has no influence on the sheath formation at the extraction grid region. This assumption is based on the following considerations:

(1) The magnetic field strength in this region is such that the weak magnetic field approximation can be used;
(2) The magnetic field lines in this region are nearly parallel to the discharge chamber axis [see Fig. 1(a)], thus crossing the electric field lines in the space charge sheath region at very small angles; this means that the $E \times B$ drift has a negligible effect on the velocity of the charged particles

A typical electric circuit schematic of an ion thruster (discharge chamber and the electrode system) is shown in Fig. 1(b). Notice that the power supplies provide the required axial potential distribution for ion beam production.

To investigate the ion optics of a multiaperture electrode system it is sufficient to examine the ion optics produced by two adjacent apertures.[11] The ion-emitting surface can be established in the same way as that for a solid emitter in order to extract an ion beam from the plasma as shown in Fig. 2. The radius of curvature of the emitting surface (space charge sheath) can be derived from the spherical diode concept[12]
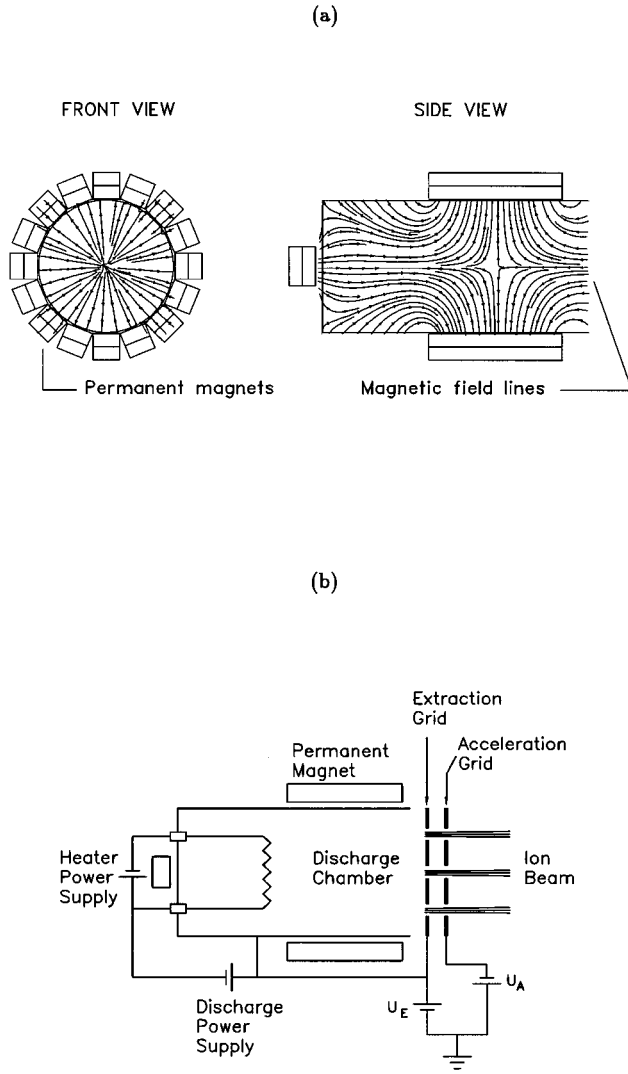
FIG. 1. The 5 cm ion thruster schematics: (a) magnet assembly geometry with the magnetic field lines and (b) electric circuit.

$$R_\Sigma = 1.6 l_T \left(\frac{P_0}{P_0 - P_j} \right), \qquad (1)$$

where the normalized perveances P_j and P_0 are given by

$$P_j = \frac{j_\Sigma}{U_T^{3/2}} \qquad (2)$$

and

$$P_0 = \frac{5.5 \times 10^{-12}}{l_T^2} \left(\frac{q}{M} \right)^{1/2}, \qquad (3)$$

where

$$j_\Sigma = j_0 / \phi_0 \qquad (4)$$

is the current density at the emitting surface and

$$j_0 = (q/2MU_N)^{1/2} F/A_0 \qquad (5)$$

is the ion beam current density related to a thrust F and a net applied potential U_N. The electrode transparency is evaluated as
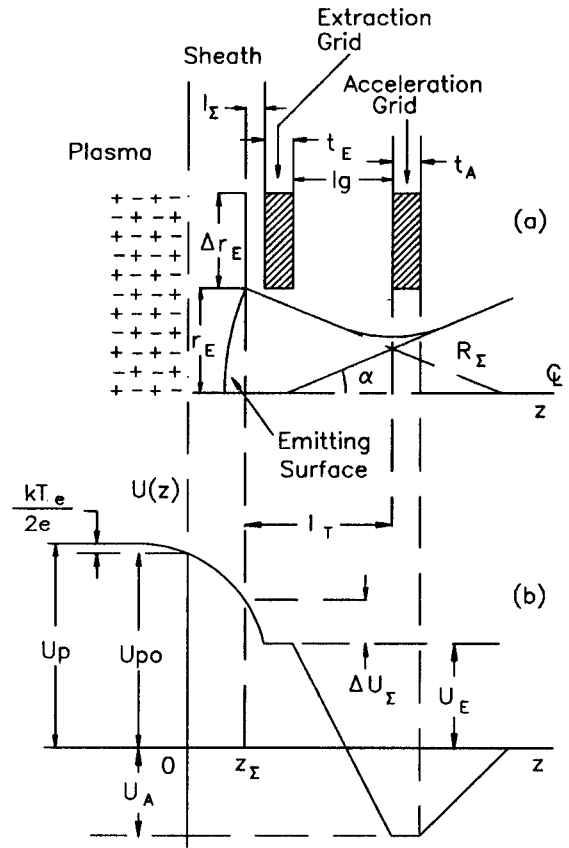

FIG. 2. (a) Emitting-surface parameters and electrode system along with geometrical parameters and (b) the potential axial profile schematic.

$$\phi_0 = N_A \left(\frac{r_E}{r_0} \right)^2. \qquad (6)$$

Equation (1) shows that the ion-emitting surface will be concave ($R_\Sigma > 0$) if $P_j < P_0$, convex ($R_\Sigma < 0$) if $P_j > P_0$, and plane ($R_\Sigma \rightarrow \infty$) if $P_j = P_0$.

The potentials associated with the electrode system are all related to a voltage ratio R which is given by[10]

$$R = \frac{U_N}{U_T} = \frac{\Delta U_\Sigma + U_E}{U_N + |U_A|}, \qquad (7)$$

where U_N and U_T are the net and total voltages.

Substituting Eq. (5) in Eq. (4) and combining the resulting equation for j_Σ with Eq. (1), the radius of curvature is rewritten as

$$R_\Sigma = \frac{1.6 l_T}{1 - 4.05 \times 10^{10} \dfrac{F}{\phi_0 R^{1/2}} \left(\dfrac{l_T}{r_0 U_T} \right)^2}, \qquad (8)$$

where R is given by Eq. (7) and the total acceleration distance l_T (see Fig. 2) is expressed by

$$l_T = l_g + t_E + l_\Sigma, \qquad (9)$$

where $l_\Sigma = z(U_E) - z(U_\Sigma)$ denotes the distance from the emitting surface to the extraction electrode. The parameter l_Σ depends on the potential difference between the emitting surface and the extraction electrode (Fig. 2). Such a dependence

can be roughly obtained from the Langmuir–Child law for a plane diode which gives $l_\Sigma \approx (\Delta U_\Sigma^{3/2}/j_\Sigma)^{1/2}$. However, if ΔU_Σ is not known then neither the distance l_Σ nor the total acceleration length can be determined. To do so, the Poisson equation for the axial coordinate z is used by considering both the electron and the ion charge densities in the sheath region. A typical potential distribution from the plasma to the region downstream to the acceleration electrode is shown in Fig. 2. Assuming a Maxwellian energy distribution for electrons, the electron density variation in the sheath is[10]

$$n_e(z) = n_{e0} \exp\left(\frac{e[U(z) - U_{p0}]}{kT_e}\right), \tag{10}$$

where n_{e0} is the electron density at the sheath edge where $U(z) = U_{p0}$, so that

$$n_{e0} = \frac{j_\Sigma}{e v_{i0}} = \frac{j_0}{e \phi_0 v_{i0}} \tag{11}$$

and v_{i0} is the ion acoustic velocity, as required by the Bohm criterion:

$$v_{i0} = \sqrt{kT_e/M}. \tag{12}$$

The potential at the beginning of the sheath (see Fig. 2) is given by

$$U_{p0} = U_p - \frac{kT_e}{2e}. \tag{13}$$

The plasma density at the beginning of the sheath is $n_{e0} = e^{-1/2} n_{ep}$ where n_{ep} is the plasma bulk density. The plasma potential can be estimated from the balance of charged particle creation and loss, which yields,[13]

$$U_p = U_E + \frac{kT_e}{e}\left\{3.76 - \ln\left[\frac{A_i}{\sqrt{Z_i}A_e}\left(2 + \frac{\sigma_0}{\sigma_i} + \frac{\delta_{se}A_p}{V_p \sigma_i n_o}\right)\right]\right\}, \tag{14}$$

where Z_i is the atomic number of the neutral atom and n_o is the neutral atom density. The primary electron leak area is given by[13,14] $A_p = 2r_p N_m L_m$ while the plasma electron leak area is $A_e = 4N_m L_m \sqrt{r_e r_i}$; r_k is the Larmor radius given by $r_k = m_k v_k / q_k B_0$, where the subscript k denotes the charged particle under consideration ($k=p$ for primary electron, $k=e$ for plasma electron, and $k=i$ for ions). The total ion leak area is given by $A_i = A_0 \phi_0 + A_c + A_f + A_{im}$, where A_c is the cathode surface area, $A_f = \beta \pi r_d^2$ is the floating surface area, β is a scaling constant, and r_d is the discharge chamber radius. The magnetic cusp ion leak area can be estimated by $A_{im} = 4A_e$.[13,14]

From energy conservation and the flux continuity condition, the ion density in the sheath is determined as[9]

$$n_i(z) = n_{e0}\left[\frac{2q}{Mv_{i0}^2}[U_{p0} - U(z)] + 1\right]^{-1/2}. \tag{15}$$

Substituting Eqs. (10)–(12) and (15) in the Poisson equation

$$\frac{d^2\Psi}{dz^2} = \frac{e}{\epsilon_0}(n_e - n_i)$$

gives the potential variation through the sheath, which is related to the axial coordinate by

$$z = \left(\frac{\epsilon_0}{2en_{e0}T_e}\right)^{1/2} \int_{U_{p0}}^{U(z)}\left\{\left(e^{\frac{e(\Psi - U_{p0})}{kT_e}} - 1\right)\right.$$
$$\left. + \left\{\left[\frac{2e}{kT_e}(U_{p0} - \Psi) + 1\right]^{1/2} - 1\right\}\right\}^{-1/2} d\Psi. \tag{16}$$

Note that the electron temperature is a parameter which has influence on the sheath formation and thus must be taken into account in the ion beam analysis.

With the above equations the emitting surface can be specified in terms of its position and radius of curvature as function of the thrust, potentials, and electrode parameters. If the interelectrode spacing is known, the total acceleration distance can be easily determined. It is possible to estimate an optimum acceleration distance such that the ion beam divergence angle is zero at the entrance to the acceleration grid aperture. This can be done using the equation for the divergence angle obtained from the spherical diode concept,[12]

$$\alpha = 0.17 \frac{d_E}{l_T}\left[1.0 - 3.98 \frac{l_T}{R_\Sigma}\right](\text{rad}), \tag{17}$$

where $d_E = 2r_E$ is the extraction aperture diameter. The divergence angle is related to the remaining ion beam parameters as shown in Fig. 2. Setting $\alpha = 0$ in Eq. (17) the optimum ratio R_Σ/l_T is

$$\frac{R_\Sigma}{l_T} = 4. \tag{18}$$

Substituting Eq. (18) in Eq. (8) yields the optimum total acceleration length:

$$l_T = 3.85 \times 10^{-6} r_0 U_T \sqrt{\frac{\phi_0}{F}}. \tag{19}$$

Hence, the optimum electrode spacing l_g can now be calculated from Eq. (9) as function of the sheath position l_Σ, and, therefore, as function of the voltage drop ΔU_Σ, once the thickness of the electrodes is specified. Note that the radius of curvature and divergence angle are both independent of the ion mass if the thrust is specified.

The procedure for obtaining the input parameters for the SLAC code is as follows. First, the plasma potential is determined as a function of a given neutral atom density using Eq. (14) and the ion drift velocity [Eq. (12)] is calculated once the electron temperature is fixed. The potential at the sheath is calculated using Eq. (13). Equation (16) is then numerically integrated in the range of $U_{p0} - U_E$ and the potential and position of the emitting surface are found in a region where the electron density is such that $n_e(l_\Sigma) = Cn_{e0}$. The constant is limited to $C \leqslant 0.2$ in order that the emitting surface is placed in a region where the space charge is mainly due to ions. This defines the emitting surface for producing the ion beam. Having found the distance and potential for the emitting surface, the optimum interelectrode spacing [Eqs. (19) and (9)] and total voltage [Eq. (7)] can be calculated. Finally, the radius of curvature of the emitting surface [Eq. (18)] is estimated for a given thrust and extraction electrode transparency [Eq. (6)].

The input parameters for the SLAC code are, therefore, as follows: the extraction and acceleration electrode voltages, U_E and U_A, the corresponding thicknesses t_E and t_A, the ion initial kinetic energy $E_i = M v_i^2/2 = M v_{i0}^2/2 + e(U_{p0} - U_\Sigma)$, the interelectrode spacing l_g, the emitting-surface voltage $\Delta U_\Sigma + U_E$, radius of curvature R_Σ, and the position l_Σ. In order to use the starting option of a spherical emitter in Herrmannsfeldt's code, the perveance of the ion beam is estimated from Eq. (2) as follows:

$$P_e = \frac{j_0 A_b}{\phi_0 \Delta U_\Sigma^{3/2}} \, [\text{A/V}^{3/2}], \tag{20}$$

where $A_b = \pi(r_E + \Delta r_E)^2$ is the electrode ion impingement area, r_E is the extraction electrode radius, and Δr_E is an increment on the electrode radius in order to take into account the metallic region of the extraction electrode, as shown in Fig. 2. P_e is thus held constant for all iterative cycles.

III. ELECTRODE DESIGN METHOD RESULTS

A. Doubly charged ion production

Before presenting the electrode system of the 5 cm ion thruster, the rate of doubly charged ion production will be assessed. Doubly charged ions constitute a significant lifetime problem for inert-gas ion thrusters.[15] Moreover, such ions are undesirable as their presence reduces the overall thruster efficiency and invalidates the simple relationship between ion beam current and thrust as stated in Eq. (5).

The set of equations for determining the sheath parameters is derived assuming that the plasma contains only one ion species. Nevertheless there are some situations where this condition is not achieved since doubly and singly charged ions can be created in the plasma. When multicharged ion species are present in a plasma the ion flux through the space charge sheath is no longer described by the Langmuir–Child three-halves power law. In this case the radius of curvature of the emitting surface cannot be given by Eq. (1) since the source term in the Poisson equation should be modified to include all the plasma particles. The double-to-single ion current ratio is given by[16]

$$\frac{I_{++}}{I_+} = \frac{K F_{++}}{2 P_0^+} \sqrt{\frac{8 k T_0}{\pi e T_e}} \, \phi_0 A_0 j_0 \, \frac{(e V_D - \phi_2)}{\dot{m}(1 - \eta_u)}, \tag{21}$$

where for $K = 3.0 \times 10^{-15}$ m^3/(eV s) and $P_0^+ = 1.4 \times 10^{-13}$ m^3/s for xenon, $F_{++} = 7$,[16] T_0 is the temperature of the neutral atoms, V_D is the discharge voltage, $\phi_2 = 23.0$ eV,[16] and $\dot{m}(1 - \eta_u) = e v_0 A_0 \phi_0 n_0/4$ is the neutral atoms loss rate (v_0 is the thermal velocity of the neutral atoms).

Assuming $\phi_0 = 0.57$, $A_0 = 1.96 \times 10^{-3}$ m^2, and $j_0 = 9.7$ A/m^2, Eq. (21) is rewritten as

$$\frac{I_{++}}{I_+} = 1.21 \times 10^{-5} \sqrt{\frac{T_0}{T_e}} \frac{(e V_D - 23.0)}{\dot{m}(1 - \eta_u)}. \tag{22}$$

However, the double-to-single ion current ratio in the exhaust ion beam is also related to the ratio of number densities of the corresponding species in the discharge chamber by[16,17]
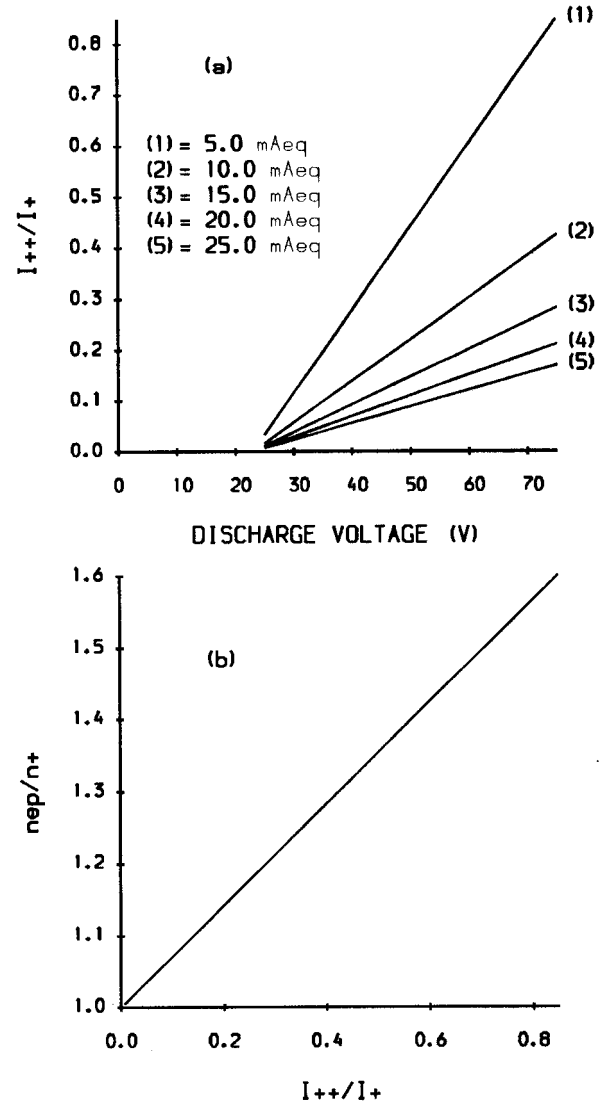

FIG. 3. (a) Doubly-to-singly charged ion current ratio and (b) the ratio of plasma density to singly charged plasma ion density at $T_e = 10$ eV.

$$\frac{I_{++}}{I_+} = 2^{3/2} \frac{n_{++}}{n_+}. \tag{23}$$

From the plasma neutrality condition ($n_{ep} = n_+ + 2 n_{++}$) and Eq. (23) the ratio of the plasma density to the singly charged ion density is

$$\frac{n_{ep}}{n_+} = 1 + \frac{\sqrt{2}}{2} \frac{I_{++}}{I_+}. \tag{24}$$

From Eqs. (22) and (24) it is possible to determine the discharge voltage range and the neutral atom loss rate yielding values of I_{++}/I_+ low enough to validate the singly charged plasma ion approach. The ratio I_{++}/I_+ is plotted as a function of the discharge voltage for different neutral loss rates in Fig. 3(a) for $T_e = 10$ eV and in Fig. 4(a) for $T_e = 3$ eV. These two electron temperature values were utilized on the basis of results from Ref. 18. Note that if $I_{++}/I_+ \lesssim 0.1$, then $n_{ep}/n_+ \approx 1$ as indicated in Figs. 3(b) and 4(b). Such low values are obtained for a discharge voltage of less than 55 V at $T_e = 10$ eV and less than 40 V at $T_e = 3$ eV for a xenon

TABLE I. Electrode system parameters extracted from Ref. 10.

Electrode spacing ratio l_g/d_E	0.5
Extraction electrode diameter d_E	12.7 mm
Extraction electrode thickness t_E	2.2 mm
Number of apertures N_A	7
Voltage ratio R	0.7
Total voltage U_T	1100 V
Plasma potential U_p (relative to U_E)	42.0 V
Electron temperature T_e	7.8 eV
Normalized perveance per hole	2.5×10^{-9} A/V$^{3/2}$
Propellant	argon

$l_\Sigma = 327.0$ μm from the extraction electrode with a radius of curvature of $R_\Sigma = 20.3$ mm. By adding the extraction electrode thickness (t_E) to this sheath position the emitting surface is localized at a normalized distance $z/d_E = 0.2$ in the coordinate system of Ref. 10. Therefore, the theoretical and experimental results are in close agreement as the radius of curvature obtained here is only 3.8% larger than the measured value of Ref. 10. This validates the use of the spherical diode concept to obtain both the theoretical emitting-surface position and radius of curvature.

C. Electrode system for the 5 cm ion beam

The design values of Table II were used to estimate the emitting-surface parameters. The electron and ion leak areas were estimated using: $B_0 = 0.1$ T, $N_m = 17$, $L_m = 5.0$ cm, $r_d = 2.5$ cm, $\delta_{es} = 0.5$, and $\beta = 0.25$.[4] The elastic cross section was $\sigma_0 = 20.65 a_0^2$ and the inelastic cross section was $\sigma_i = 5.5\pi a_0^2$ for 50 eV primary electrons,[20,21] whereas they were $\sigma_0 = 18.7 a_0^2$ and $\sigma_i = 4.4\pi a_0^2$, respectively, for 30 eV primary electrons.[20,21]

The plasma potential [Eq. (14)] was found to lie between 908.9 and 932.7 V for the 3–10 eV electron temperature range and a xenon neutral atoms loss rate of 25 mA$_{eq}$ (corresponding to a neutral atom density of 1.7×10^{18} m^{-3})[4] for $V_D = 50$ V. On considering a 30 V discharge voltage the plasma potential is within the 904.7–918.8 V interval at $\dot{m}(1-\eta_u) = 5.0$ mA$_{eq}$ ($n_0 = 3.5 \times 10^{17}$ m^{-3}) for the same electron temperature range.

The position and potential of the emitting surface have been found using the parameters listed in Table II for the range $0.1 \leq n_e(z)/n_{e0} \leq 0.35$. The resulting emitting-surface
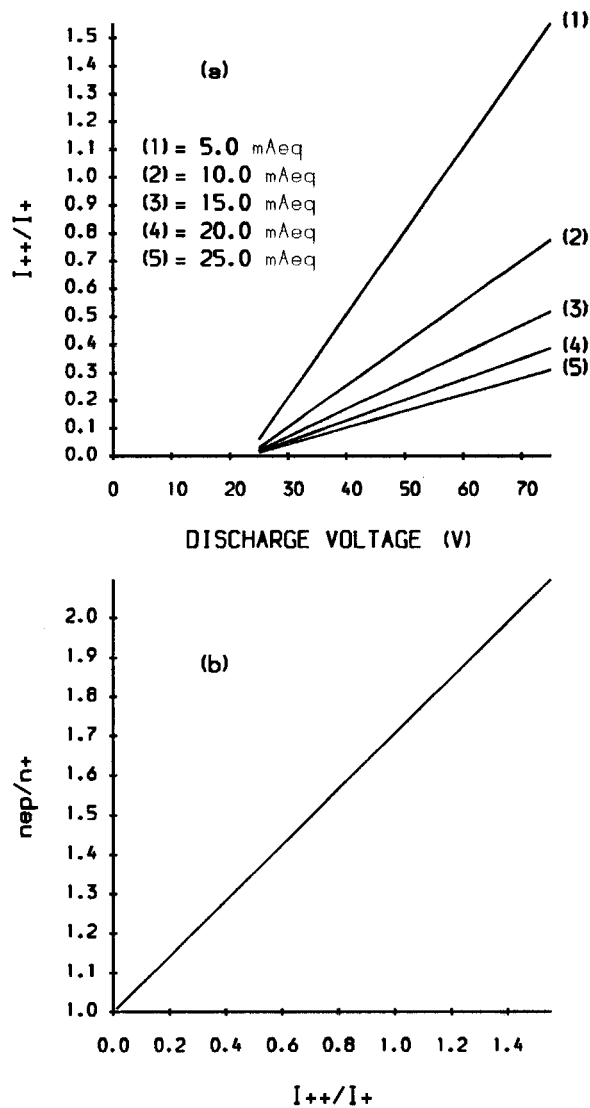
FIG. 4. (a) Doubly-to-singly charged ion currents ratio and (b) the ratio of plasma density to singly charged plasma ion density at $T_e = 3$ eV.

neutral loss rate of 25 mA eq. If the neutral atoms loss rate is reduced to 5 mA eq the discharge voltage must be less than 30 V for the electron temperatures considered in this paper. This result agrees with the statements of Ref. 19.

B. Test case

In order to check the validity of the analytical model, a theoretical emitting surface has been determined using the data extracted from Ref. 10 which is given in Table I. The experimentally measured plasma parameters for singly charged plasma ions[10] are consistent with the electrode geometry and applied voltages.

The radius of curvature has a geometrically estimated value $R_\Sigma = 21.1$ mm for the outermost equipotential surface at $z/d_E = 0.2$, where $n_e = 0.1 n_{e0}$ in Ref. 10. For $U_T = 1100$ V and $R = 0.7$, Eq. 7 gives $U_N = 770$ V and $|U_A| = 330$ V. Choosing $U_A = -330$ V in order to have the potential distribution as depicted in Fig. 2 and solving consistently the set of equations of Sec. II, the theoretical emitting surface for an electrode transparency $\phi_0 = 0.64$ is found to be positioned at

TABLE II. Five centimeter ion thruster parameters for the multi-aperture two-electrode system.

Ion beam radius (r_0)	25 mm
Number of apertures per electrode (N_A)	499
Extraction aperture diameter (d_E)	1.7 mm
Electrode transparency (ϕ_0)	0.57
Extraction electrode thickness (t_E)	0.1 mm
Acceleration electrode thickness (t_A)	0.5 mm
Diameter ratio (d_A/d_E)	1.0
Extraction electrode voltage U_E	900 V
Acceleration electrode voltage U_A	−100 V
Electron temperature T_e	3 to 10 eV
Discharge voltage V_D	30 to 50 V
Thrust (F)	1 mN
Propellant	xenon

TABLE III. Electrode system parameters calculated for the 5 cm ion thruster.

V_D	50				30		V
T_e	3		10		3	10	eV
n_e/n_{e0}	0.1	0.2	0.1	0.2	0.35	0.26	
lg	2.1	2.2	2.1	2.2	2.1	2.1	mm
l_Σ	3.9	22.4	14.2	39.3	1.1	1.5	μm
R_Σ	8.9	10.2	8.9	10.2	8.9	8.9	mm
U_Σ	900.5	902.6	904.6	911.6	900.0	900.3	V
ΔU_Σ	0.5	2.6	4.6	11.6	0.0	0.3	V
U_T	1000.5	1002.6	1004.6	1011.6	1000.0	1000.3	V
R	0.9	0.9	0.9	0.9	0.9	0.9	

parameters, namely, potential, position, and radius of curvature are given in Table III. The optimum electrode spacings for the assumed electron temperature values are also listed in Table III. Simulation results of the full system obtained using the estimated ion beam parameters from Table III are presented in Fig. 5 for $n_e/n_{e0}=0.1$ and in Fig. 6 for $n_e/n_{e0}=0.2$, assuming $V_D=50$ V. The behavior of the extracted ion beam is quite insensitive to the electron temperature, as shown in Figs. 5(a) and 5(b), if the emitting surface is very close to the extraction electrode. Major differences in the ion beam behavior arise if the emitting surface is located far from the extraction electrode as illustrated in Figs. 6(a)
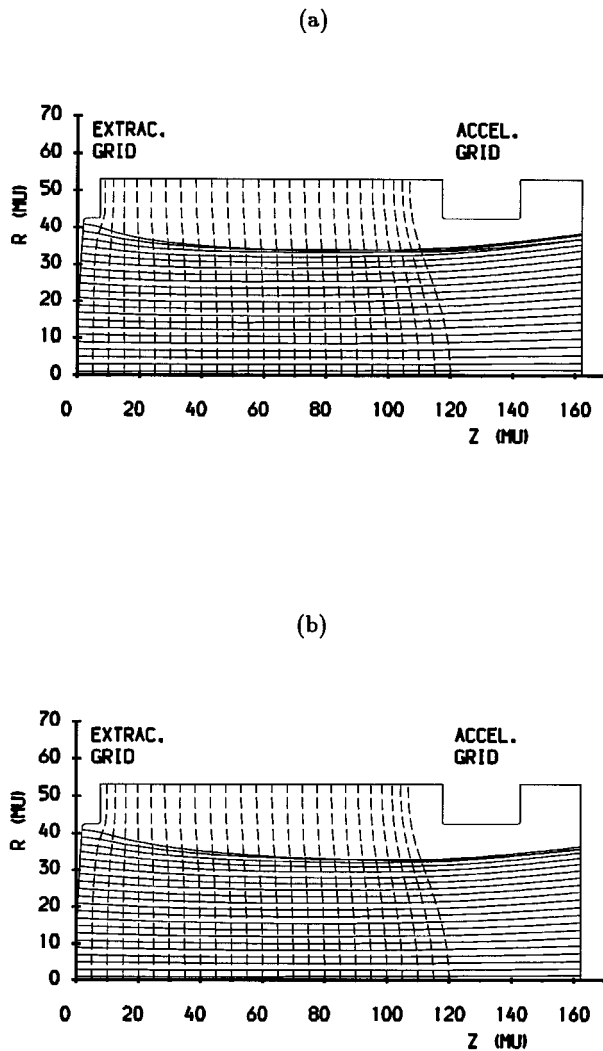
(a)

(b)

FIG. 5. Ion beam trajectories and equipotential lines corresponding to the optimum interelectrode spacing (Table III) for (a) $T_e=3$ eV and (b) $T_e=10$ eV assuming $V_D=50$ V and $n_e/n_{e0}=0.1$. Radial and axial scales are calibrated in mesh units, where 50 MU = 1.0 mm.
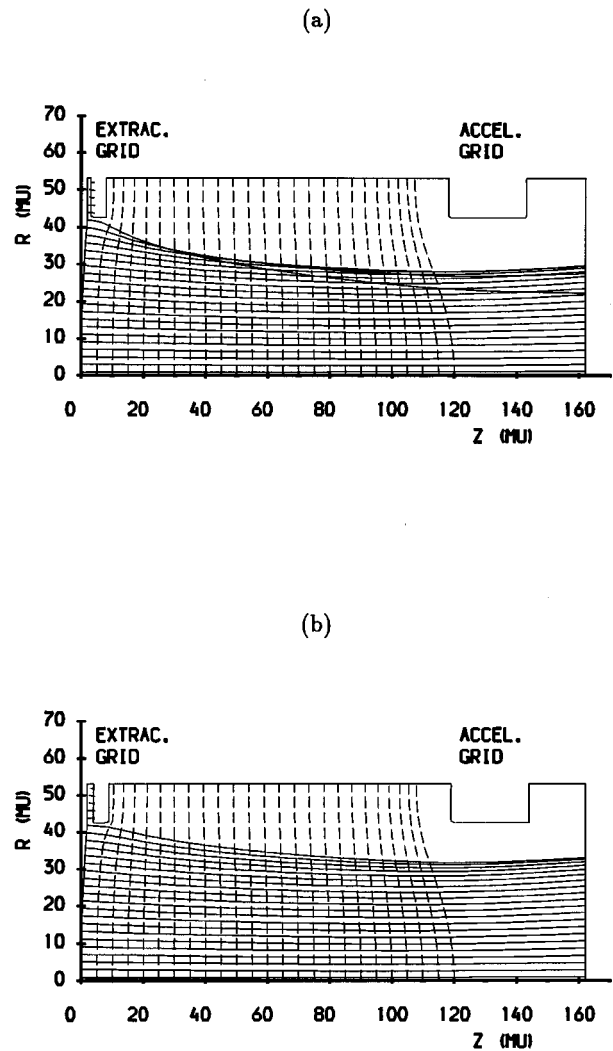
(a)

(b)

FIG. 6. Ion beam trajectories and equipotential lines corresponding to the optimum interelectrode spacing (Table III) for (a) $T_e=3$ eV and (b) $T_e=10$ eV assuming $V_D=50$ V and $n_e/n_{e0}=0.2$. Radial and axial scales are calibrated in mesh units, where 50 MU = 1.0 mm.
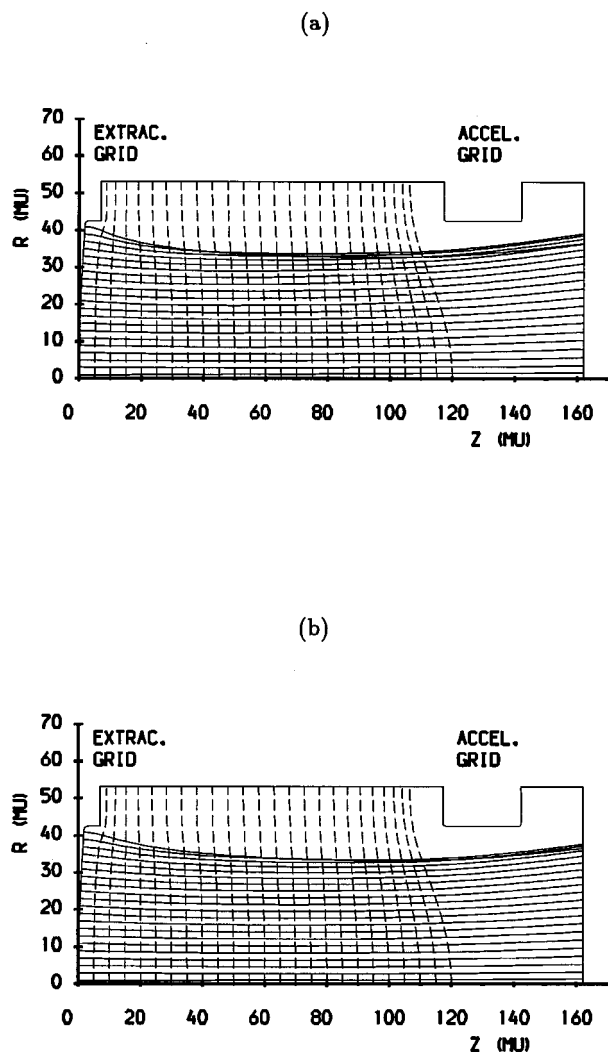
(a)

(b)

FIG. 7. Ion beam trajectories and equipotential lines corresponding to the optimum interelectrode spacing (Table III) for (a) $T_e = 3$ eV ($n_e/n_{e0} = 0.35$) and (b) $T_e = 10$ eV ($n_e/n_{e0} = 0.26$) assuming $V_D = 30$ V. Radial and axial scales are calibrated in mesh units, where 50 MU=1.0 mm.

and 6(b). In the latter case, a lower electron temperature gives beamlets having more crossing trajectories as shown in Fig. 6(a).

As the discharge voltage is decreased to $V_D = 30$ V, the outermost emitting surface is located in a region where $n_e/n_{e0} = 0.35$ for an electron temperature of 3 eV and where $n_e/n_{e0} = 0.26$ for $T_e = 10$ eV. This means that a thin plasma sheath is formed if the discharge voltage is lowered (Fig. 7). In this case, the ion beam has a similar behavior to that already shown in Fig. 5(a) and there is hardly any significant differences between the two beams at electron temperatures of 3 and 10 eV as shown in Figs. 7(a) and 7(b).

Note that the divergence angle is nearly zero for the beam envelope at the entrance of the acceleration electrode as shown in Figs. 5–7. This can be explained by observing that the interelectrode spacing and the radius of curvature of the emitting surface are weakly dependent on the electron temperature (Table III). The closer to the extraction electrode the emitting surface is, the larger the divergence angle becomes at the exit of the acceleration electrode.
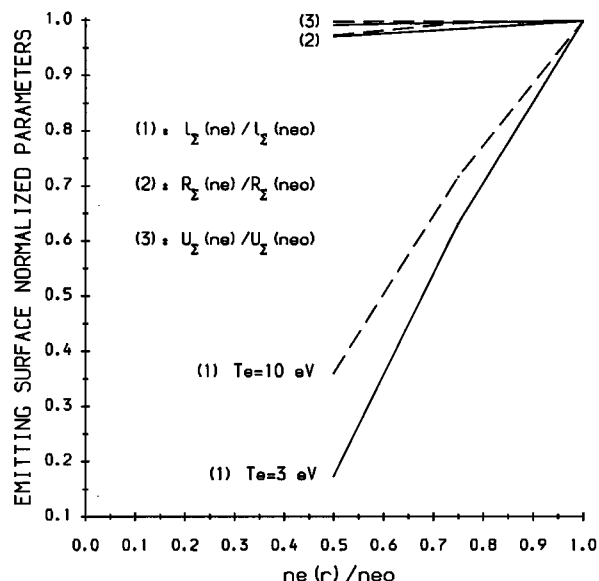

FIG. 8. The effect of radial variation of the plasma density on the normalized plasma emitting surface parameters $R_\Sigma(n_e)/R_\Sigma(n_{e0})$, $l_\Sigma(n_e)/l_\Sigma(n_{e0})$ and $U_\Sigma(n_e)/U_\Sigma(n_{e0})$, for $V_D = 50$ V and two values of the electron temperature.

The plasma density distribution along the radial distance in the discharge chamber of ion thrusters is nonuniform. The effects on R_Σ, l_Σ, and U_Σ of varying the plasma density along the radial coordinate are shown in Fig. 8, where the normalized variables refer to $R_\Sigma(n_e)/R_\Sigma(n_{e0})$, $l_\Sigma(n_e)/l_\Sigma(n_{e0})$, and $U_\Sigma(n_e)/U_\Sigma(n_{e0})$ (n_{e0} being the centerline plasma density at the sheath edge). The normalized radius of curvature and potential are always above 0.94 whereas the normalized distance between the emitting surface and the extraction electrode decreases as the plasma density is lowered for both electron temperatures assumed in this work. The effect on the ion beam of decreasing the plasma density is the same as that of bringing the emitting surface closer to the extraction grid. The individual ion beams produced by the multiaperture electrode system will have different shapes along the radial distance. They can be represented qualitatively in Fig. 5(a) for the outer apertures, in Fig. 6(a) for the intermediate apertures, and in Fig. 6(b) for the inner apertures. In any case, there is no beam interception by the acceleration electrode. These plots clearly show how the ion beam optics are affected by the electron temperature, discharge voltage, and emitting-surface location.

IV. DISCUSSION

A simple analytical approach was developed for the design of ion beam extraction and acceleration grid systems of ion thrusters consistent with the plasma production in the discharge chamber.

The determination of the emitting surface for the ion optics of a multiaperture electrode system has shown that the ion beam extraction takes place in a region where the ions play a prominent role on space charge sheath formation.

The divergence angle is found to be nearly zero at the entrance to the acceleration electrode when the optimum

electrode spacing is used. In addition, it has been demonstrated that the plasma electron temperature has a strong influence on the ion beam laminarity.

Beam simulations have indicated that erosion of the acceleration electrode by ion impact does not occur for the potentials and electrode geometry considered in this work. The extracted current is about 80% of the total current at the extraction electrode, showing that the designed ion-optical system is well suited for the space applications of the 5 cm ion thruster.

ACKNOWLEDGMENT

NOMENCLATURE

A_b	total ion impingement area
A_e	plasma electron leak area on magnetic cusps
A_i	total plasma ion leak area
a_0	Bohr radius
A_p	primary electron leak area on magnetic cusps
B_0	surface magnetic induction of permanent magnet
E_p	primary electron energy
F	thrust j_0 ion beam current density
l_g	interelectrode spacing
l_T	total acceleration length
l_Σ	emitting surface-to-extraction electrode gap
L_m	magnetic cusp length
M	ion mass
m_e	electron mass
N_m	number of magnetic cusps
N_a	number of electrode apertures
n_{e0}	electron density at the plasma sheath edge
n_{ep}	electron density at the plasma bulk
n_i	ion density
P_e	extraction aperture perveance
q	electric charge
r_E	extraction electrode aperture radius
R_Σ	emitting surface radius
r_0	overall ion beam radius
T_e	electron temperature
t_a	acceleration electrode thickness
t_E	extraction electrode thickness
U_A	acceleration electrode voltage
U_A	extraction electrode voltage
U_p	plasma potential
U_T	total voltage
$U(z)$	potential at axial position z
U_ϵ	emitting-surface potential
V_p	plasma volume
v_{i0}	ion drift velocity
z	axial coordinate
z_ϵ	emitting surface axial position
δ_{es}	secondary electron emission coefficient
ϕ_0	extraction electrode geometrical transparency
ϕ_2	threshold energy for production of doubly charged ion
σ_i	primary electron inelastic cross section
σ_0	primary electron elastic cross section

[1] Proceedings of the 5th International Conference on Ion Sources, Beijing, China, 31 August–4 September 1993 [Rev. Sci. Instrum. **65** (April, 1994)].

[2] V. K. Rawlin, AIAA Paper 91-3567, 1991.

[3] Special Issue on Electric Propulsion [J. Brit. Interp. Soc. **41** (April/May, 1988)].

[4] G. M. Sandonato, I.E.E.E. Trans. Plasma Sci. (to be published).

[5] R. Becker and W. Herrmannsfeldt, Rev. Sci. Instrum. **63**, 2756 (1992).

[6] S. Fu, A. Kitagawa, and S. Yamada, Rev. Sci. Instrum. **65**, 1435 (1994).

[7] X. Peng, W. Ruyten, and D. Keefer, AIAA Paper 91-0607 (1991).

[8] W. B. Herrmannsfeldt, Electron Trajectory Program, Stanford Linear Accelerator Center, California University, SLAC Report No. 226, November 1979.

[9] G. M. Sandonato, Doctoral thesis, Instituto Tecnológico de Aeronáutica (ITA), São José dos Campos, SP, Julho 1993.

[10] G. Aston and P. J. Wilbur, Prog. Astron. Aeronaut. **79**, 251 (1984).

[11] A. T. Forrester, Large Ion Beams—Fundamentals of Generation and Propagation (Wiley, New York, 1988), p. 117.

[12] J. R. Coupland, T. T. Green, D. P. Hammond, and A. C. Riviere, Rev. Sci. Instrum. **44**, 1258 (1973).

[13] C. Chan, T. Intrator, and N. Hershkowitz, Phys. Lett. **91A**, 167 (1982).

[14] K. N. Leung, N. Hershkowitz, and K. R. MacKenzie, Phys. Fluids **19**, 1045 (1976).

[15] M. J. Patterson, AIAA paper 92-3202, July 1992.

[16] H. Kaufman and R. S. Robinson, AIAA paper 79-205, Oct. 30–Nov. 1, 1979.

[17] R. R. Peters, P. J. Wilbur, and R. P. Vahrenkamp, J. Spacecraft **14**, 461 (1977).

[18] J. R. Brophy and P. J. Wilbur, AIAA J. **24**, 1516 (1986).

[19] J. S. Sovey, J. Spacecraft **21**, 488 (1984).

[20] F. J. de Heer, R. H. Jansen, and W. Van de Ray, J. Phys. B **12**, 979 (1979).

[21] D. Raap and P. E. Golden, J. Chem. Phys. **43**, 1464 (1965).